A core driver of somatic markers: Interoception shapes the transition of decision making

Shogo Yonekura[1*†], Hoshinori Kanazawa[1†], Atsushi Narita[1], Yasuo Kuniyoshi[1]

[1]Graduate School of Information Science and Technology, The University of Tokyo, Tokyo & 113-8656, Japan.

[*]Corresponding author. Email: {yonekura/kanazawa/kuniyosh}@isi.imi.i.u-tokyo.ac.jp

[†]These authors contributed equally to this work.

A multitude of brain regions exhibit synchronized activity in conjunction with cardiorespiratory and gastric processes. This study demonstrates the mutual influence of interoception and perceptual decision-making processes, with a particular focus on the phenomenon of human binocular rivalry. Combining this finding with computational modeling and mathematical analysis, we show that a common interoceptive input to competing neurons can control the transition probability of fixed decisions. The Somatic Marker Hypothesis (SMH) proposes that interoception is essential for adaptive coordination of the decision process to reach a rational decision. Our results revealed a fundamental mechanism underlying the SMH.

Decision making is influenced by interoception, which refers to information from internal organs. Three decades ago, the Somatic Marker Hypothesis (SMH) was proposed, which states that interoceptive information is important for rational decision-making. Without interoceptive information, humans are inclined to adhere to irrational decisions (*1–4*). The original SMH postulates that internal organs calculate the emotional value of a stimulus or situation, e.g. whether it is positive or negative, and send the value information back to the brain. The decision-making neural circuit, which receives the value information from the body, then modifies the decision output. A substantial

body of research has been conducted using the methodology of a gambling task and reinforcement learning to gain insight into how interoception reflects the emotional valence of a decision and how those interoceptive information affect the decision-making process (*2, 4, 5*). Nevertheless, the neurodynamical mechanism by which interoception affects decision-making has remained unclear.

Recent research has shown that the activity of the cardiorespiratory and gastrointestinal systems entrains the rhythm of a variety of brain regions, affecting cognitive activities such as memory, attention, and perceptual decision-making, as well as physical behaviors (*6–18*). These findings have prompted a reframing of SMH from the perspective of a dynamical system, rather than from the framework of reinforcement learning.

A neural circuit for behavioral decision making is typically composed of competing neurons or neuronal ensembles with self-excitatory connections and mutual inhibitory connections (*19–22*). This motif circuit often behaves as a winner-take-all (WTA) system, where a single neuron or ensemble of neurons dominates the circuit while the others are silenced. The same WTA motif is observed in a neural circuit for perceptual decision making such as binocular rivalry (*23*). This evidence suggests that the basic neural dynamics underlying SMH and binocular rivalry are analogous. To this end, we approach SMH by investigating how interoceptive signals influence brain dynamics and decision making using a binocular rivalry task.

Mutual effects of human perceptual decision making and the interoception

The frequency of perceptual alternation in binocular rivalry is modulated by respiratory rate (*24*). To gain a deeper understanding of the interaction between perceptual decision making and internal organs, we measured respiratory chest motion, electrocardiogram (ECG), and pupil diameter during human binocular rivalry. Then the phase of chest movement $\theta(t)$ corresponding to the respiratory phase, the cardiac R-wave $R(t)$, the normalized pupil diameter $d_p(t)$, the blink timing $B_l(t)$, the perceptual switching time e_p were calculated (Fig. 1-(A, B), Supplementary Text).

The likelihood of a perceptual alternation event, e_p, given the respiratory phase θ and rate (slow, normal, fast) was estimated using the Markov Chain Monte Carlo (MCMC) method (*25*) on data

from 30 male participants (mean age is 25.5 with a standard deviation of 2.8). Fig. 1-(C) shows the mean and 95 % highest density interval (HDI) of the estimated likelihood function $\hat{p}(e_p|\theta)$. It is evident that $\hat{p}(e_p|\theta)$ depends on the respiration phase θ and that the shape of $\hat{p}(e_p|\theta)$ is influenced by the respiration rate.

The information flows between e_p, θ, R, d_p and B_l are estimated using a method for calculating the transfer entropy (TE) between point processes (*26*). The variables $\theta(\in [0, 2\pi])$ and $d_p(\in [0, 1])$ of the nonpoint process have been converted to point processes (see Method). The heatmap in Fig. 1-(D) shows the p-values obtained from the permutation tests using the point-process TE described in Ref. (*26*). P-values less than 0.05 are indicated by red, double-underlined text. The results indicate that there is a significant flow of information from the respiratory phase and the cardiac R-wave to the perceptual alternation, irrespective of the breathing rate instruction (slow, normal, or fast).

The vector of embedding dimensions (l_x, l_y) is a parameter that indicates how many spikes are used to compute the TE from the source process y to the target process x. It should be noted that the respiratory phase θ has a significant information flow with $l_y \geq 10$ with $x = 2, 3$ in slow and normal breathing rates. This implies that one cycle of breathing has a significant contribution to two and three perceptual switching events, in slow and normal breathing rates (*27*). In contrast, at fast breathing rate, TE was only significant for $l_x < 3$. This implies that at fast breathing rate, breathing has only a short term influence.

It should be noted that in fast breathing rate, we found significant information flows from the occurrence of perceptual alternation to the respiration phase, the R-wave, and the pupil diameter, and blink events. Likewise, we found a significant flow of information from blinking to perceptual switching at normal and fast breathing rates, but such information flow disappeared at slow breathing rates. See also Fig.S3-S5, where we show the results of the TE permutation test computed with different TE parameters and wider pairs of embedding dimensions (I_x, I_y). Furthermore, see Supplementary Text for the discussion of a weak parameter sensitivity of the TE permutation.

Overall, these results demonstrate that the most combinations of perceptual alternation, respiration phase, R-wave, pupil diameter, and blink exert a significant influence on one another (except from pupil diameter to perceptual alternation and blink).

Interoceptive dynamics shape the probability of decision switching

The minimal model that can account for the perceptual alternation observed in binocular rivalry is a stochastic bistable system (*23, 28–30*). While the currently most detailed model of binocular rivalry proposes the necessity of hierarchical connection, the simplest stochastic bistable model still represents the majority of the characteristics of human perceptual alternation (*23, 30*). In this paper, we examine a stochastic coupled neural system comprising self-excitatory and lateral inhibitory connections. For the sake of simplicity in mathematical analysis, we do not consider hierarchical feedback connections. The model is described as

$$\tau \frac{d\mathbf{X}}{dt} = -\mathbf{X} + f\left(g(t), \mathbf{W}\mathbf{X}\right) + A(t) + \sqrt{2D}\xi(t), \tag{1}$$

where $\mathbf{X} = \left(\begin{smallmatrix} x_1 \\ x_2 \end{smallmatrix}\right)$, $\mathbf{W} = \left(\begin{smallmatrix} w_{11} & -w_{12} \\ -w_{21} & w_{22} \end{smallmatrix}\right)$, and $\xi = \begin{pmatrix} \xi_1 \\ \xi_2 \end{pmatrix}$, and $f(g(t), x) = 1/(1 + \exp(-g(t)\,x))$. Note that $g(t)$ is the activation function of a neuron, reflecting the effect of the neuromodulator (described in further detail below). Additionally, the condition $g(t) > 0$ must be satisfied for the neurons to retain bistability and WTA capability. x_i (where the indices i and j are 1 or 2) denotes the membrane state of ith neuron, $f(x)$ denotes the sigmoidal activation function of a neuron which roughly corresponds to the firing rate of a neuron, w_{ii} and w_{ij} represents the weight of self-excitatory and mutual-inhibitory synaptic connections, respectively. $\sqrt{2D}\xi(t)$ denotes the Gaussian noise with the standard deviation of D. When the self-excitatory coupling of neurons is sufficiently strong, the network has two fixed points and exhibits the characteristics of WTA behavior (Fig. 2-(A–C)). (Hereafter in this paper, we used $\tau = 5$ [ms] for any numerical simulations).

The precise model for the coupling of internal organs and cortical neurons has yet to be identified. Nevertheless, at least for the coupling of cortical activity and breathing, a number of mechanisms have been proposed (*16*); (a) neuromodulation of cortical neurons by the locus coeruleus, which receives respiratory information (*5, 31–36*), and (b) the broadcast of respiratory sensory information to cortical neurons via the olfactory bulb (*8, 37, 38*). Based on these arguments about the influence of breathing, we have postulated that interoception in general (not limited to respiration) affects this

WTA circuit in two ways, via neuromodulation $g(t)$ and additive sensory input $A(t)$, as follows

$$g(t) = g_g \sin 2\pi f t + g_b, \tag{2a}$$

$$A(t) = A_g \sin 2\pi f t + A_b. \tag{2b}$$

Fig. 2-(D) shows the typical switching behavior of WTA in synchrony with the periodic neuromodulation $g(t)$. If $g_g = 0$ and $g_b > 0$, it represents the static activation gain; a high value of g_b, i.e., $g_b \gg 0$, results in a deeper double-well potential landscape, thereby, impeding the transition from the fixed states (Supplementary Text, and Fig. S2).

It should be noted that the model described in this paper is highly simplified and comprises only the most essential and minimal components. Consequently, the analysis and discussion presented below are applicable regardless of the anatomical complexity of the actual brain, or whether the decision is perceptual or behavioral, provided that the behavior of the brain or the decision-making process is reduced to stochastic bistable dynamics.

Fig. 2-(E) depicts the mean switching count per second, C_{sw}, as a function of the neuromodulator bias, g_b, and the gain, g_g. The figures were generated with $D = 0.01$ (for $f = 0.1$, 1, and 5 Hz), and $D = 0.1$ (for $f = 5$ Hz). It is important to note that the parameter space for $C_{sw} > 0$ is linear with respect to g_b and g_g, regardless of the noise intensity D. The switching probability of the winner-neuron is a function of the frequency and phase of the interoceptive neuromodulator, as well as the input noise intensity. It is crucial to acknowledge that interoception at high frequency does not significantly contribute to the state transition of a decision-making neural system. This is evidenced by the observation that higher interoceptive frequency, with $f = 5$ Hz and $D = 0.01$, results in a smaller swtching count C_{sw} than $f = 1$ Hz and $D = 0.01$.

Fig. 2-(F) demonstrates that the switching of the winning neuron is likely to occur at a specific phase, contingent on the interoceptive frequency. The precise mechanism underlying the pronounced jitters in $f = 1$ remains uncertain. For low frequency ($f = 0.1$ Hz) and small values of g_b, the probability distribution of $p(e_p|\phi)$ exhibits multimodality and subsequently converges to a unimodal distribution. Under both effects of $g(t)$ and $A(t)$, the multimodal distribution of $p(e_p|\phi)$ was observed. Furthermore, Fig. 2-(F) shows that the peak of $p(e_p|\phi)$ is shifted with respect to g_b by the influence of the interoceptive neuromodulator $g(t)$. The peak shift of $p(e_p|\phi)$ by g_b and A_b is also shown in Fig. 3-(A,B).

The interoceptive phase alters the positive/negative feedback mode of a WTA circuit We present a straightforward mathematical analysis of the impact of the interoceptive neuromodulator. We can assume that the time constant τ in Eq. 1 is $\tau = 1$ without any loss of generality (*39*). By taking the Taylor expansion of Eqs. 1 and 2 with $x_i \sim 0$, we immediately obtain the linear differential equation with respect to $\mathbf{X}$ as

$$\frac{d\mathbf{X}}{dt} = -\mathbf{X} + \frac{1}{2}\mathbf{W} + \frac{1}{4}\left(g_b + g_g \sin 2\pi f t\right)\mathbf{W}\mathbf{X} + \sqrt{2D}\xi(t). \tag{3}$$

Eq. 3 implies that the dynamics of $\mathbf{X}$ is inverted from negative feedback to positive feedback based on the phase of the periodic neuromodulator, and the periodic switching of the feedback modes occurs when $g_g > 4 - g_b w_{ii}$ (note that the index i denotes either 1 or 2, and therefore w_{ii} denotes the excitatory self-coupling). If we introduce the phase of interoceptive signal as $\phi = 2\pi f t$ [rad], the WTA neurons behave in the negative feedback mode within the range $\pi \leq \phi \leq 2\pi$ and attempt to maintain the current state and with respect to $\mathbf{X}$, and within the range $0 \leq \phi \leq \pi$, WTA neurons behave in the positive feedback mode and amplify the minor fluctuations, leading to the reversal of a winning neuron. Furthermore, the linearity of the conditions for the feedback modes switching (i.e., $g_g > 4 - g_b w_{ii}$) is observed as a linear distribution of $C_{sw} > 0$ with respect to g_b and g_g. This is shown in Fig. 2-(E).

Interoceptive sensory input exerts influence on the higher-order activity of a WTA The effect of interoceptive sensory input is highly nonlinear with respect to several parameters of the interoceptive sensory input. The nonlinearity with respect to the interoceptive phase ϕ is shown in Fig. 3-(B), and similarly, the nonlinearity with respect to the gain A_g and the bias A_b is shown in Fig. 4, which shows the averaged switching number C_{sw} per second with respect to A_g and A_b of the interoceptive sensory input with $D = 0.1$ and $g(t) = 1$. Moreover, it should be noted that the shape of the region in which the switching count is positive (i.e., $C_{sw} > 0$) undergoes a significant transformation contingent on the signal frequency.

The nonlinear effect of $A(t)$ on decision switching becomes more apparent through the analytical treatment based on Itô's formula (*40*). When $g_g = 0$ and $g_b \sim 0$, the WTA circuit behaves linearly, and in this regime the common input of $A(t)$ does not contribute at all to the dynamics of the neural state transition (Supplementary Text). If the activation gain g_b is sufficiently large, the magnitude

relation of the decision output, i.e., $F(x_1, x_2) = f(x_1) - f(x_2)$, is nonlinearly affected by $A(t)$ as

$$F(x_1, x_2) = \int_0^t \left(4g_b^2 \left(x_1^2 - x_2^2\right) A(s) + H(x_1, x_2)\right) ds + \frac{\Delta_f^2}{2} \int_0^t \eta^2(s)\, ds + \Delta_f \int_0^t \eta dW_t + C, \tag{4}$$

where $H(x_1, x_2)$ is a function of x_1 and x_2, $\eta = \sqrt{2D}\xi$, C is an integral constant, $\Delta_f^2 = \partial^2 f(x_1)/\partial x_1^2 - \partial^2 f(x_2)/\partial x_2^2$, and $\Delta_f = \partial f(x_1)/\partial x_1 - \partial f(x_2)/\partial x_2$. It is shown that $F(x_1, x_2)$ receives the quadratic negative feedback effect $(x_2^2 - x_1^2)$ when $A(t)$ is in the phase $[0, \pi]$ and similarly, the positive feedback effect in the phase $[\pi, 2\pi]$. For the detailed derivation and explanation of Eq. 4, see Supplementary Text.

Comparing human data and model behavior If we simply compare Fig. 1-(C) and Fig. 2-(F), it might be possible to naively claim that the shape difference of $p(e_p|\theta)$ with breathing rate (slow, normal, fast) is mainly based on the different effect of the interoceptive neuromodulator $g(t)$ or the interoceptive sensory input $A(t)$ rather than on the interoceptive frequency f; human perceptual switching is dominated by $A(t)$ at normal breathing rate, dominated by $g(t)$ at fast breathing rate, and dominated by both $g(t)$ and $A(t)$ at slow breathing rate. Separating the contribution of interoceptive neuromodulation and sensory input to perceptual alternation will require a new methodology.

Interoception is all SMH needs

A WTA circuit is a general model of a cortical column circuit, perceptual decision making, and behavioral decision making A WTA circuit is a motif network that is ubiquitous in a brain and observed at both the local and global levels. A cortical column structure consists of coupled local WTA circuits (*41–43*). And the brain forms competing neural networks at the global level. This is evidenced by the existence of neural circuits that induce binocular rivalry or behavioral decision-making, which consist of a competing network at the global level (*20, 23, 28, 30*).

Neurons in a WTA circuit are likely to share the same interoceptive information. Information about the internal body is transmitted through the autonomic nerve systems, via the spinal cord or

several small nuclei such as the nucleus tractus solitarii (NTS) in the brain stem (*5, 44, 45*). This evidence suggests that interoceptive signals are compressed by the autonomic nervous system, and neurons in a global or local WTA circuit receive the same compressed interoceptive information.

Value information can be fully encoded by the interoceptive raw signal Our numerical and theoretical results show that a common interoceptive raw signal can control the switching probability of the winner of WTA neurons. This further indicates that interception can directly represent the value information for a decision circuit by using the signal frequency and bias. For example, if the current decision is marked as negative, then the decision must be flexible, and this requirement is met by breathing slowly and deeply so that $C_{sw} > 0$ in Fig. 3. Conversely, if the decision is marked positive by the body, the current decision must not change, and this requirement is met by breathing quickly and shallowly so that $C_{sw} \sim 0$. We speculate that the interoceptive signals from internal organs are sufficient to realize human SMH.

Conclusion

The present study showed that perceptual decisions in binocular rivalry and interoceptive signals such as respiration, cardiac R-wave are influencing each other. Numerical and mathematical analyses showed that a common input of an interoceptive signal can control the transition probability of the decision output of a competing neural circuit. These findings suggest that interoceptive dynamics is a core driver that adaptively coordinates the decision-making process to achieve rational behaviors.

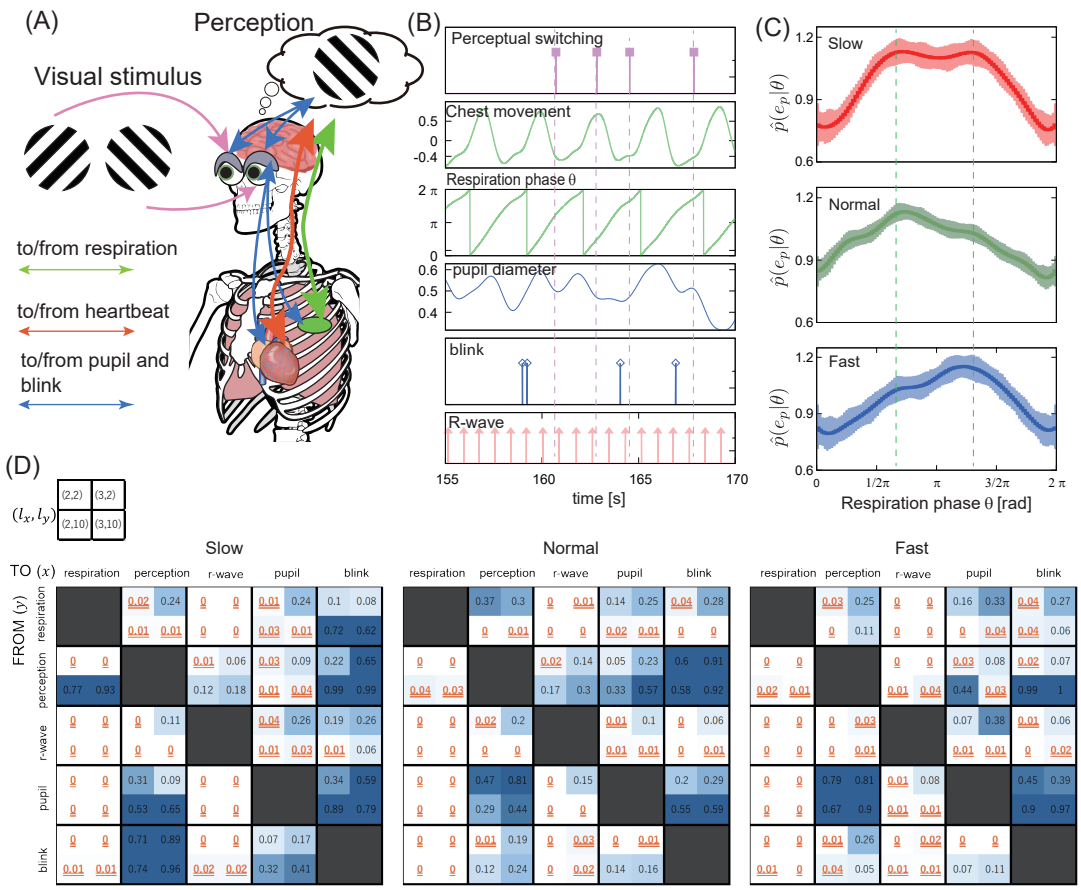

Figure 1: **Mutual influence of human perceptual alternation and interoception.** **(A)** The experimental setup to understand the interoceptive effect on the perceptual decision process in binocular rivalry. Stripe patterns with different angles are presented to the left and right eye of a participant. A participant is instructed to breathe at a normal/slow/fast rate and to press the left/right button when viewing the left/right image and both buttons when viewing both images. The respiratory phase θ, the cardiac R-wave denoted by R, the normalized pupil diameter d_p, the blink timing B_l, and the perceptual switching timing e_p are computed based on the output of the chest belt sensor, the electrocardiogram (ECG), and the pupilometer, respectively **(B)**. **(C)** The estimated likelihood of perceptual alternation in human participants with respect to the respiration rate (slow, normal, fast) and the respiration phase θ with the 95 % highest density interval (HDI). **(D)** The heatmap shows the p-values obtained by means of the permutation test using transfer entropy (TE) between θ, e_p, R, d_p, and B_l. The 2×2 submatrix denotes the embedding dimension l_x, l_y used to compute TE from $y \rightarrow x$. The p-values which satisfy the condition < 0.05 are indicated by red text with a double underline.

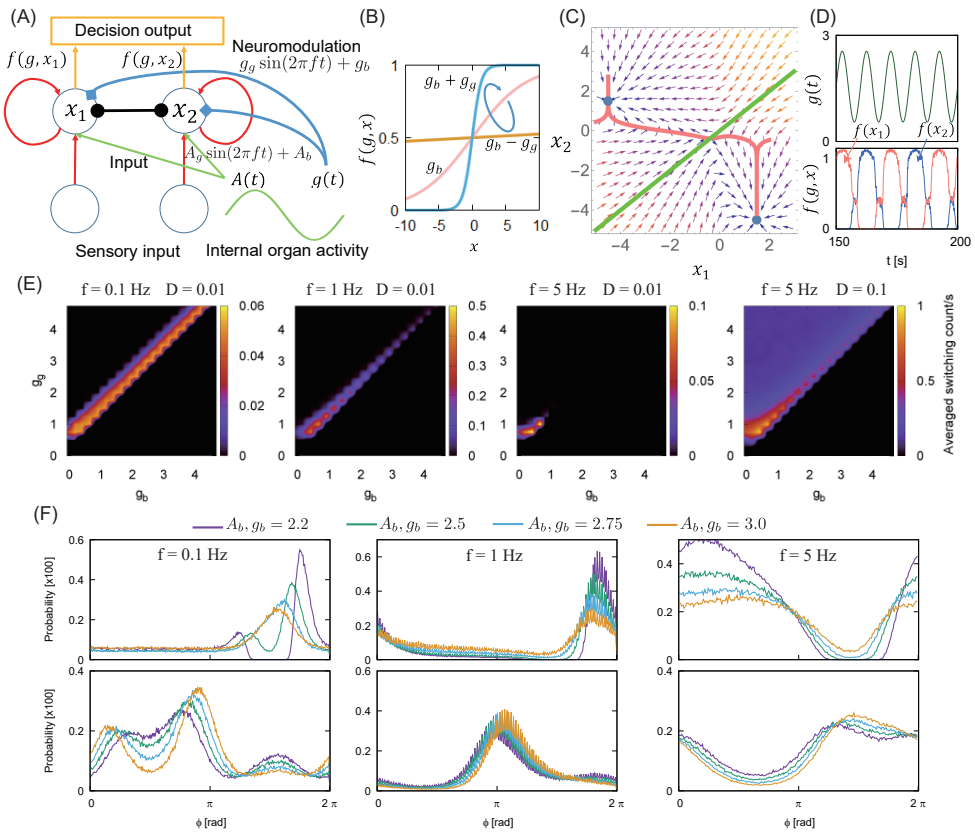

Figure 2: **A model of perceptual/behavioral decision making coupled with interoception. (A)** A neural model used to analyze the interoceptive effect on the decision-making process. **(B)** The output of a neuron is determined by the sigmoidal function $f(g, x)$ where $g(t)$ is driven periodically by the neuromodulator within the range $[g_b - g_g, g_b + g_g]$. If the self-excitatory connection is strength enough, the WTA circuit has double-well potential well, and the vector field of x_1 and x_2 have two fixed points described by the blue circles as the panel **(C)**. The green line is $x_2 = x_1$, and when the system $\mathbf{X}$ is above the line $x_2 = x_1$, the system converges to the fixed points around $(-4, 2)$, and around $(2, -4)$ otherwise. **(D)** is the typical example of the system driven with common interoceptive signal, where the green trajectory denotes $g(t)$. Red and blue lines are the output of the x_1 and x_2, respectively. It is shown that the switching timing of a winning neuron are tightly locked to the interoceptive phase. **(E)** Color maps of averaged switching count per second, C_{sw}, with respect to the bias g_b and gain g_g, of the neuromodulation. **(F)** The probability distribution of the switching likelihood $p(e_p|\phi)$ with respect to the phase ϕ of the activity of an internal organ. The internal organ activity is transmitted to neurons via neuromodulation $g(t) = g_g \sin(2\pi f t) + g_b$ (top column) and sensory input $A(t) = A_g \sin(2\pi f t) + A_b$ (bottom column). Note that $p(e_p|\phi)$ is normalized as $\int_0^{2\pi} p(e_p|\phi) d\phi = 1$. We used $D = 0.01$ for the panel (D) and $D = 0.1$ for the panels (F).

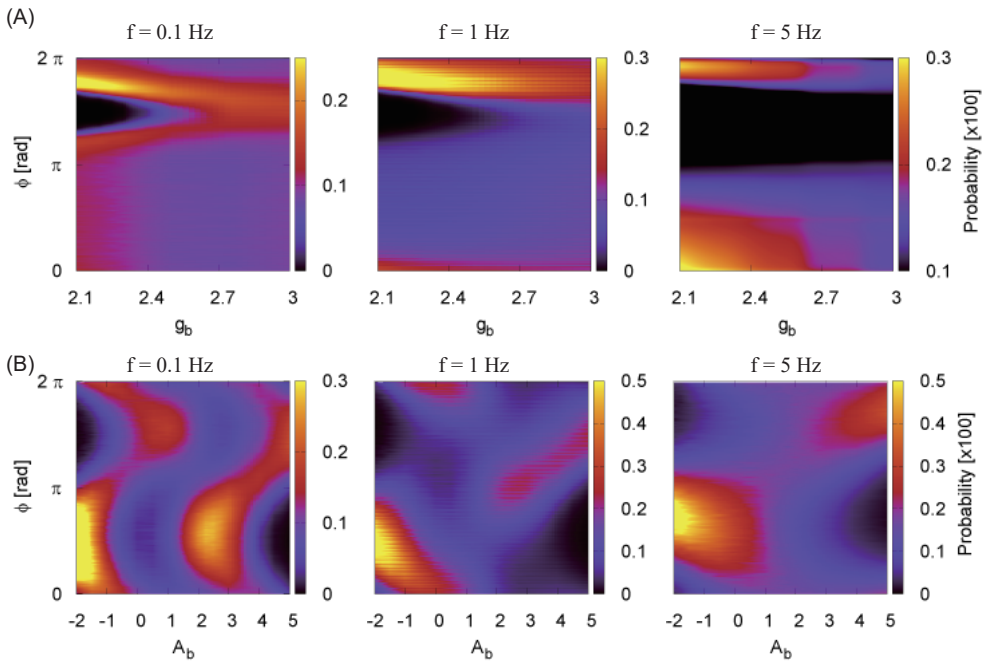

Figure 3: **The color maps of the probability density function of the likelihood $p(e_p|\phi)$ (multiplied by 100) , with respect to g_b.** Note that $p(e_p|\phi)$ is normalized with respect to each different value of g_b. **(A)** The figures in the top row were obtained by utilizing the interoceptive neuromodulator $g(t)$. We employed $g_g = 2$ and $D = 0.2$. Note that $g(t)$ must be greather than zero, and therefore $g_b > 0$. **(B)** Similarly, the bottom figures were obtained by utilizing interoceptive sensory input $A(t)$ and $D = 0.1$. Note that $A(t)$ is not restricted to positive values. Therefore, A_b can be < 0, in contrast to g_b.

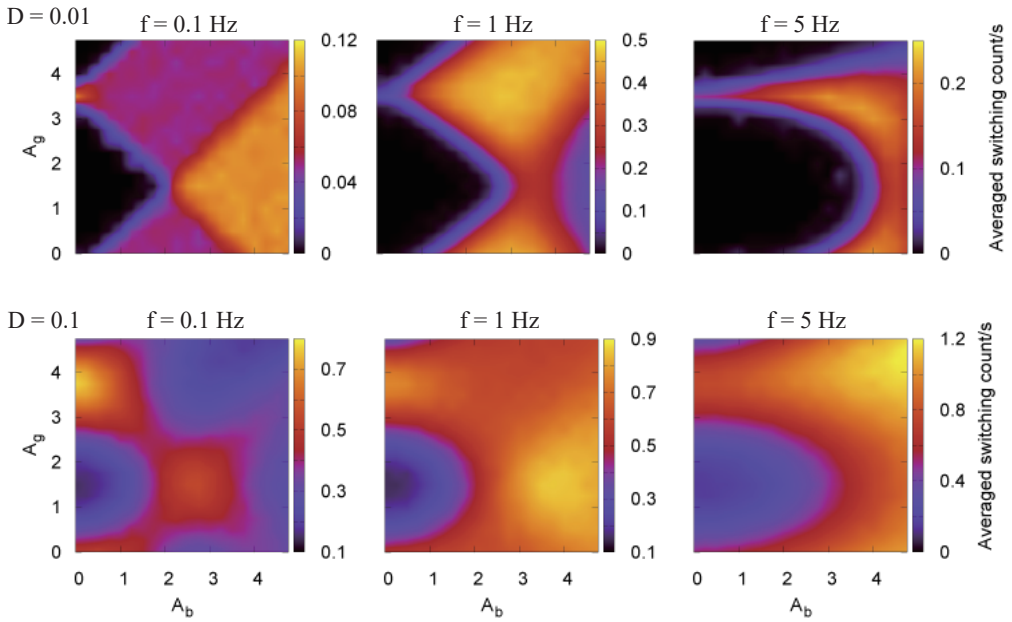

Figure 4: **The averaged switching counts per second C_{sw} [Hz] with respect to the parameters of interoceptive sensory input A_g and A_b, noise intensity D and the input frequency f.** The parameter space for $C_{sw} > 0$ was highly nonlinear with respect to A_g and A_b. Furthermore, it was observed that the shape of the parameter space for C_{sw} deforms with the noise intensity D.

References and Notes

1. A. R. Damasio, ed., *Descartes' Error* (Putnam Adult, New York, USA) (1994).

2. A. Bechara, A. R. Damasio, The somatic marker hypothesis: A neural theory of economic decision. *Game Econ. Behav.* **52**, 336–372 (2005).

3. L. K. Fellows, M. J. Farah, Different underlying impairments in decision-making following ventromedial and dorsolateral frontal lobe damege in humans. *Cereb. Cortex* **15**, 58–63 (2005).

4. B. D. Dunn, T. Dalgleish, A. D. Lawrence, The somatic marker hypothesis: A critical evaluation. *Neurosci. Biobehav. Rev.* **30**, 239–271 (2005).

5. T. Poppa, A. Bechara, The somatic marker hypothesis: revisiting the role of the 'body-loop' in decision-making. *Curr. Opin. Behav. Sci.* **19**, 61–66 (2018).

6. S. N. Garfinkel, *et al.*, Fear from the heart: Sensitivity to fear stimuli depends on individual heartbeats. *J Neurosci* **34** (19), 6573–6582 (2014).

7. S. N. Garfinkel, H. D. Critchley, Threat and the body: How the heart supports fear processing. *Trends Cogn. Sci.* **20** (1), 34–46 (2016).

8. C. Zelano, *et al.*, Nasal respiration entrains human limbic oscillations and modulates cognitive function. *J. Neuroscience* **36** (49), 12448–12467 (2016).

9. J. F. Thayer, A. L. Hansen, E. Saus-Rose, B. H. Johnsen, Heart rate variability, prefrontal neural function, and cognitive performance: the neurovisceral integration perspective on self-regulation, adaptation, and health. *Ann. Behav. Med.* **37**, 141–153 (2009).

10. I. Rebollo, A.-D. Devauchelle, B. Béranger, C. Tallon-Baudry, Stomach-brain synchrony reveals a novel delayed-connectivity resting-state network in humans. *eLife* **7**, e33321 (2018).

11. N. Wolpert, C. Tallon-Baudry, Coupling between the phase of a neural oscillation or bodily rhythm with behavior: Evaluation of different statistical procedures. *NeuroImage* **236**, 118050 (2021).

12. H.-D. Park, O. Blanke, Heartbeat-evoked cortical responses: Underlying mechanisms, functional roles, and methodological considerations. *NeuroImage* **197**, 502–511 (2019).

13. A. M. Herman, M. Tsakiris, Feeling in control: The role of cardiac timing in the sense of agency. *Affect. Sci.* **1**, 155–171 (2020).

14. D. S. Kluger, E. Lalestrieri, N. A. Busch, J. Gross, Respiration aligns perception with neural excitability. *eLife* **10**, e70907 (2021).

15. A. Galvez-Pol, P. Virdee, J. villacampa, J. Kilner, Active tactile discrimination is coupled with and modulated by the cardiac cycle. *eLife* **11**, e78126 (2022).

16. S. Ashhad, K. Kam, C. A. D. Negro, J. L. Feldman, Breathing rhythm and pattern and their influence on emotion. *Annu Rev Neurosci* **45**, 223–2247 (2022).

17. T. Engelen, M. Solcà, C. Tallon-Baudry, Interoceptive rhythms in the brain. *Nat Neurosci* **26**, 1670–1684 (2023).

18. J. P. Veillette, F. Gao, H. C. Nusbaum, Cardiac afferent signals can facilitate visual dominance in binocular rivalry. *eLife* **13**, RP95599 (2024).

19. J. W. Kable, P. W. Glimcher, The neurobiology of decision: Consensus and controversy. *Neuron* **63** (6), 733–745 (2009).

20. A. T. Kuan, *et al.*, Synaptic wiring motifs in posterior parietal cortex support decision-making. *Nature* **627**, 367–373 (2024).

21. M. Usher, J. D. Cohen, D. Servan-Schreiber, J. Rajkowski, G. Aston-Jones, The role of locus coeruleus in the regulation of cognitive performance. *Science* **283** (5401), 549–554 (1999).

22. G. Aston-Jones, J. D. Cohen, An integrative theory of locus coeruleus-norepinephrine function: Adaptive gain and optimal performance. *Annu. Rev. Neurosci.* **28**, 403–450 (2005).

23. R. Cao, A. Pastukhov, S. Aleshin, M. Mattia, J. Braun, Binocular rivalry reveals an out-of-equilibrium neural dynamics suited for decision-making. *eLife* **10**, e61581 (2021).

24. A. Yousef, Deep breathing governs binocular rivalry. *PsyArXiv* pp. 2146–2165 (2020), doi: 10.31234/osf.io/zr3uk.

25. J. Cook, Splines, in *PyMC examples*, P. Team, Ed., doi:10.5281/zenodo.5654871.

26. D. P. Shorten, R. E. Spinney, J. T. Lizier, Estimating transfer entropy in continuous time between neural spike trains or other event-based data. *PLOS Comput Biol* **17** (4), e1008054 (2021).

27. The point process Y corresponding to the respiration phase θ with $I_y = 10$ denotes one cycle of respiration; for we computed the point process by dividing the parameter space $\theta : [0, 2\pi]$ into 10 subspaces. See Supplementary Text for more details.

28. Y.-J. Kim, M. Grabowecky, S. Suzuki, Stochastic resonance in binocular rivalry. *Vision Res* **46**, 392–406 (2005).

29. M. T. Cuello, A. Drew, A. S. S. Jose, L. M. Fernández, S. Soto-Faraco, Alpha fluctuations regulate the accrual of visual information to awareness. *Cortex* **147**, 58–71 (2022).

30. A. W. Freeman, Multistage model for binocular rivalry. *J Neurophysiol* **94** (6), 4412–4420 (2005).

31. M. C. Melnychuk, *et al.*, Coupling of respiration and attention via the locus coeruleus: Effects of meditation and pranayama. *Psychophysiolgy* **55** (9), e13091 (2017).

32. L. T. Lopes, *et al.*, Anatomical and functional connections between the locus coeruleus and the nucleus tractus solitarius in neonatal rats. *Neuroscience* **324**, 446–468 (2016).

33. M. C. Quintero, R. W. Putnam, J. M. Cordovez, Theoretical perspectives on central chemosensitivity: CO_2/H_2-sensitive neurons in the locus coeruleus. *PLoS Comput Biol* **13** (12), e1005853 (2017).

34. D. de Carvalho, *et al.*, Participation of locus coeruleus in breathing control in female rats. *Respiratory Physiol. & Neurobiol.* **245**, 29–36 (2017).

35. Y. Oyamada, D. Ballantyne, K. Mückenhoff, P. Scheid, Respiration-modulated membrane potential and chemosensitivity of locus coeruleus neurones in the in vitro brainstem-spinal cord of the neonatal rat. *J. Physiol.* **513** (2), 381–398 (1998).

36. K. Yackle, *et al.*, Breathing control center neurons that promote arousal in mice. *Science* **355**, 1411–1415 (2017).

37. D. H. Heck, *et al.*, Breathing as a fundamental rhythm of brain function. *Front. Neural Circuits* **10**, Article 115 (2017).

38. L. M. Kay, P. Lazzara, How global are olfactory bulb oscillations ? *J. Neurophysiol* **104** (3), 1768–1773 (2010).

39. The time-constant τ in Eq.1 can be removed by applying adequate scaling of $\mathbf{X}$ and t, and we have $d\hat{\mathbf{X}}/d\hat{t} = -\hat{\mathbf{X}} + f(\hat{\mathbf{W}}\hat{\mathbf{X}}) + \hat{A}(\hat{t}) + \hat{D}\xi(\hat{t})$, where $\hat{\cdot}$ represent the scaled variable.

40. K. Itô, On a formula concerning stochastic differentials. *Nagoya Math. J.* **3**, 55–65 (1951).

41. R. J. Douglas, K. A. C. Martin, Neuronal circuits of the neocortex. *Annu Rev Neurosci* **27**, 419–451 (2004).

42. W. Maass, To spike or not to spike: That is the question. *Proceedings of the IEEE* **103** (12), 2219–2224 (2015).

43. S. Klampfl, W. Maass, Emergence of dynamic memory traces in cortical microcircuit models through STDP. *J. Neurosci.* **33** (28), 11515–11529 (2013).

44. W. G. Chen, *et al.*, The emerging science of interoception: Sensing, integrating, interpreting, and regulating signals within the self. *Trends Neurosci* **44** (1), 3–16 (2021).

45. B. E. Kearney, R. A. Lanius, The brain-body disconnect: A somatic sensory basis for trauma-related disorders. *Front Neurosci* **16**, 1015749 (2022).

46. A. L. Goldberger, *et al.*, PhysioBank, PhysioToolkit, and PhysioNet: components of a new research resource for complex physiologic signals. *Circulation* **101** (23), e215–e220 (2000).

Acknowledgments

Funding: This research is supported by Toyota Central R&D Labs., Inc.

Author contributions: Conceptualization, S. Y., A. N., H. K. and Y. K.; methodology, S. Y., A.N. H. K., and A. N.; data curation, H. K. and A. N.; formal analysis, S. Y., A. N., and H. K.; funding acquisition; Y. K.; project administration, Y. K.; resources, Y. K. and H. K.; software, S. Y. and A. N.; validation, H. K. and Y.K.; writing and reviewing; S. Y., H. K., and Y. K.; All authors above read and agreed to the published version of the manuscript.

Competing interests: There are no competing interests to declare.

Ethics approval and consent to participate The binocular rivalry experiments described in this paper was approved by the ethics committees of our institute. All participant for the binocular rivalry experiments signed an informed consent statement.

Supplementary materials

Materials and Methods

Supplementary Text

Figs. S1 to S5

Tables S1

References *(7-46)*

Supplementary Materials for

A core driver of somatic markers: Interoception shapes the transition of decision making

Shogo Yonekura[1†], Hoshinori Kanazawa[1†], Atsushi Narita[1], Yasuo Kuniyoshi[1]

[*]Corresponding author. Email: yonekura/kanazawa/kuniyosh@isi.imi.i.u-tokyo.ac.jp

[†]These authors contributed equally to this work.

This PDF file includes:

Materials and Methods

Supplementary Text

Figures S1 to S5

Tables S1

Materials and Methods

Experimental setup of binocular rivalry

The binocular rivalry experiment described in this paper was approved by the ethics committees of our institute. All participant for the binocular rivalry experiments signed an informed consent statement. Visual stimuli with different stripe angles are presented to the left and right eyes of a participant, and a participant is asked to press either the left or right button, or both buttons, when he/she perceives a visual image presented to the left or right eye, or a mixed image. The time of the perceptual alternation $e_p(t)$ was recorded.

The experiment started 3 minutes after the first training session. In the first session (6 minutes), a participant is asked to continue breathing at normal speed. After the 3 minutes of rest, a participant is asked to continue breathing at a fast rate. In addition, after the 3 minutes of rest, a participant is asked to breathe at a slow rate. The actual breathing rate is at the discretion of the participant, as we did not use a metronome to dictate the breathing rate. This is because the natural breathing rate must vary from person to person, and breathing at an unnatural rate may have unpredictable effects on the mental state or perceptual decision-making process.

The change in a participant's chest volume $v_0(t)$ was measured at 500 Hz using a belt sensor; DC respiratory sensor, manufactured by Miyuki Giken, Tokyo, and cardiac activity was measured by an electrocardiogram manufactured by METS, Inc. at 500 Hz. Pupil diameter was measured with an HTC VIVE Pro Eye eye tracking device at 100 Hz.

Preprocessing data for TE and MCMC analyses

In TE analysis, we need paired time series data of the source process $Y(t)$ and the target process $X(t)$. In the following, we describe the preprocessing procedure for $X(t)$ and $Y(t)$. For the MCMC analysis, we used the preprocessed data of the source $Y(t) = \theta(t)$ and $X(t) = e_p(t)$ described below.

Bandpass filters We applied the bandpass filter of $[0.03, 1.0]$ Hz to the value of a belt sensor $v_0(t)$ to obtain $v(t)$. The phase $\theta(t)$ of the chest motion is calculated from the Hilbert transform of the bandpassed signal $v(t)$ as $\theta(t) = H(v) + 1/2\pi$. Note that we add a phase shift of $1/2\pi$ so

that $\theta(t) = \pi/2$ at the peak of $v(t)$. The cardiac R-wave $R(t)$ was computed using the wavelet transform (*46*). The bandpass filter of $[0.1, 3]$ Hz is applied to the pupil diameter and we obtain $d_p(t) : [0, 1]$ by normalizing the bandpass signal. Blink times $B_l(t)$ were estimated by detecting the sudden and large fluctuation of the pupil diameter.

Cropping of paired processes of a source Y(t) and a target X(t) for artifact and transient removal The TE measure assumes that the source process $Y(t)$ and the target process $X(t)$ are stationary (*26*). However, human physiological data, especially respiration data $v(t)$, contain many artifacts, such as voluntary changes in respiration rate, belt sensor position shifts, and these artifacts create transient and nonstationary respiration data. To crop the stationary region of the paired data of $(X(t), Y(t))$, we used the time window $[T_s, T_e]$ and calculated the signal-to-noise ratio (SNR) of $Y(t)$ within the time $[T_s, T_e]$. Note that the SNR will be higher if $Y(t)$ is stationary and lower if $Y(t)$ has non-stationary characteristics, such as changes in respiratory rhythm or other artifacts. Furthermore, we assumed that if $Y(t)$ is stationary, $X(t)$ is also stationary. (To obtain enough data-length, we assumed T_s and T_e is at most 100 [s]).

The SNR is calculated as follows: We computed the power spectrum $\tilde{Y}(\omega)$ of $Y(t)$ using the Fast Fourier Transform (FFT), where ω is the frequency. We assumed that ω_s, which gives the maximum $\tilde{Y}(\omega)$, is the signal frequency of $Y(t)$. The power spectrum density P at the discrete frequency step k used in the FFT is calculated as $P(k) = |\tilde{Y}(k)/(L/2)|^2$ where L is the length of the data used in the FFT. Then the SNR is SNR $= \frac{P_S}{P_N}$, where $P_S = \sum_{q=-5}^{5} P(k_s + q)$ is the power spectrum density of the signal frequency, and P_N is the sum of the power spectrum densities other than the signal frequency, i.e., $P_N = \sum P(k) - P_S$.

We searched for the time window $[T_s^*, T_e^*]$ that satisfies SNR $> \Theta$ or otherwise gives the maximum SNR, and the paired data of the source $Y(t)$ and the target $X(t)$ are cropped by the time window $[T_s^* + T_f^X, T_e^* - T_l^X]$, where T_f^X and T_l^X indicate the time to the first and last event spike of $X(t)$ after T_s^* and before T_e^*, respectively, as shown in Fig. S2. Note that $T_f^X = 0$ and $T_l^X = 0$ if $X(t)$ is a nonpoint process.

When the respiration phase θ is a source $Y(t)$, we calculated the SNR using the respiration data $v(t)$, because the phase θ loses the information of the signal amplitude (and therefore the SNR using $\theta(t)$ has less sensitivity to detect the transient process). Furthermore, when $Y(t) = \theta(t)$

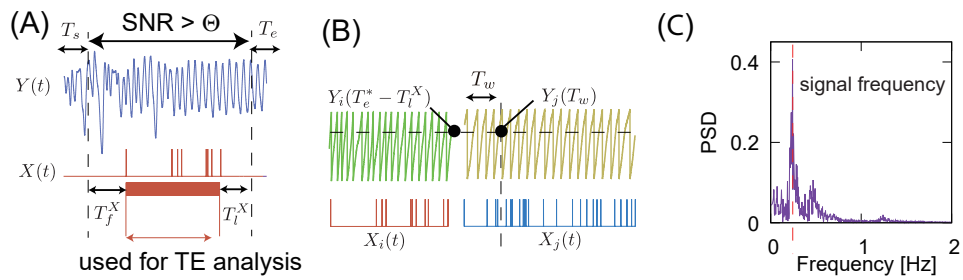

Figure S1: **Preparing data for TE and MCMC analyses (A)** The cropping procedure for the pair of source process $Y(t)$ and target process $X(t)$. We have searched for the time window $[T_s, T_e]$ that satisfies SNR $> \Theta$ or otherwise maximizes the SNR of $Y(t)$. The pair $(X(t), Y(t))$ is clipped by the time window $[T_s + T_f^X, T_e - T_l^x]$, where T_f^X and T_l^X are the time to the first and last event spikes, respectively. **(B)** $(X_i(t), Y_i(t))$ and $(X_j(t), Y_j(t))$ of the ith and jth participant are connected at the time $t = T_w$ which gives $d\left(Y_i(T_e^* - T_l^X) - Y_j(T_w)\right) \sim 0$. **(C)** A brief description of how to determine the signal frequency of $Y(t)$ by using the FFT; we assumed the signal frequency ω_s has the maximum power spectrum density (PSD) $P(\omega_s)$.

and the maximum SNR is less than 0.3, we did not use the whole $v(t)$ because it means that $v(t)$ is not stationary. Similarly, we did not use some data with a significantly low number of $\int_{t=0}^{T} e_p(t)dt$ (where $T = 6$ min is the session duration), e.g, only one perceptual alternation during a 6-min session, because it seems that the recording of $e_p(t)$ failed; we did not use the data e_p if $\int_{t=0}^{T} e_p(t)dt < 0.1M_p$, where M_p is the average number of perceptual alternations of all participants. Consequently, we collected the pair data of $(v(t), e_p(t))$ from 18 participants for normal breathing rate, 11 participants for fast breathing, and 17 participants for slow breathing out of 30 participants (30 male, mean age is 25.5 with standard deviation 2.8).

Merging the cropped data from multiple participants The cropped stationary data from different participants are merged into a time series data. To merge $Z_i = (X_i, Y_i)$ and $Z_j = (X_j, Y_j)$, we searched for T_w that satisfies $d\left(Y_i(T_e^* - T_l^X), Y_j(T_w)\right) < d_\Theta$, where $T_e^* - T_l^X$ is the last time stamp of (X_i, Y_i), $d(x, y)$ is a Euclidean distance, and $d_\Theta = 0.05$. It should be noted that this merging strategy does not break the structure of the flow of information from Y to X.

If both the source and target processes are nonpoint processes, we simply computed the Eu-

clidean distance $d(Z_i(T_e), Z_j(T_w))$ and searched for the minimum T_w that gave $d < 0.05$. If both the source and destination processes are point processes, we simply merged Z_i and Z_j at $T_w = 0$.

Converting a nonpoint process to a point process to calculate TE We computed the TE between respiration phase $\theta(t)$, cardiac R-wave $R(t)$, pupil diameter $d_p(t)$ and blinking timing $B_l(t)$ and perceptual alternation event $e_p(t)$ by using the computational method provided by Ref. (*26*). This method assumes that both source and target signals, Y and X are point-process and have the continuous time representation; $Y = \{t_0^Y, t_1^Y, \dots\}$, and $X = \{t_0^X, t_1^X, \dots\}$, where $t_i^{Y,X}$ is the timestamp of the event occurrence.

It is important to note that $R(t)$, $B_l(t)$ and $e_p(t)$ are point processes and $\theta(t)$ and $d_p(t)$ are continuous processes. Therefore, it is necessary to convert $\theta(t)$ and $d_p(t)$ to point processes. To convert the $q(t)$ of a continuous process to a point process time series $Q^p(t)$, the variable space is divided into 10 subspaces $[\Omega_0, \Omega_1, \dots \Omega_9]$. If the continuous signal $q(t)$ moves from the current subspace to another subspace at time t^q, the time stamp t^q is appended to the time series $Q^P(t)$. This results in the following representation: $Q^p(t) = \{t_0^q, t_1^q, \dots\}$.

Note that the TE value depends on the seed for the random number generator. Therefore, we calculated the TE value using 10 different random seeds. In addition, we generated 250 surrogate data for each seed. We calculated p value using 5 original TE values and 1250 surrogate TE values; $p = N_s/N_{total}$, where N_s is the number of surrogate data that have a higher TE value than the original data, and $N_{total} = 1250$.

The parameters used to calculate TE The parameters used to calculate TE are tabulated below. For detailed explanation of the parameters, see Refs. (*26*).

The parameter sensitivity of TE between point processes

The results of the permutation test using TE between point processes (*26*) have a weak sensitivity to the parameter especially k_{global} which is the parameter to determine the radius of the ϵ-ball; to explain it in a very simple way, the TE algorithm counts the number of points inside the ϵ-ball. Note that this algorithm assumes that the data points are uniformly distributed within the ϵ-ball. Therefore using too large value of k_{global} will result in incorrect TE estimation if the data length is

Table S1: **The parameters used to calculate TE.** For Fig. 1 we used $k_{global} = 5$ and $k_{perm} = 50$. The results of the permutation test using TE with $k_{global} = 2$, $k_{perm} = 100$, and $I_x = 1$ are shown in the supplementary Fig. S3–S5.

Parameter	Description	Value
I_x	Number of interspike intervals in target history embeddings	1, 2, 3
I_y	Number of interspike intervals in source history embeddings	2, 10
k_{global}	Initial number of nearest neighbors to determine the radius of the ϵ-ball	2, 5
N_X	Number of target events in the data from a participant	varied
N_U/N_X	Ratio of random samples used to estimate the unconditional probability density of the target process	10, 1
$N_{surrogates}$	Number of surrogates data	250
k_{perm}	number of nearest neighbours used in the local permutation tests	100, 50
D_k	Small noise intensity added to construct the embedding vector (x, y)	10^{-8}

not long enough.

The supplementary Fig. S3–S5 shows the differences of the p-values computed with $k_{global} = 2$ and 5. It is shown that $k_{global} = 2$ marks the information flows as significant in more combinations of the embedding dimensions (I_x, I_y) than $k_{global} = 5$. Ref. (*26*) argues that both $k_{global} = 2$ and 5 have sufficient accuracy to detect and reject the significant and insignificant information flows if the data length is long enough. The difference in p values for different (I_x, I_y) induced by k_{global} in our analysis of the human data may reflect the data length limitation. Note that the different p values induced by k_{global} do not affect our main results that there are significant mutual information flows between perceptual alternation and interoception.

Numerical simulations of WTA

The data shown in Fig. 3 were obtained by using the results of 50 trials of a 10^5 s numerical simulation. The stepsize of a numerical simulation was 1 [ms], and a different random seed was used in each simulation trial. The human perceptual state has at least three states: left-image dominant (L), right-image dominant (R), or mixed (LR). The transition between these three states in numerical simulations using a WTA circuit can be represented by using the variable of $F(x_1, x_2) =$

$f(x_1) - f(x_2)$. However, we have defined only two states L: $F(x_1, x_2) > 0.5$ and R: $F(x_1, x_2) < -0.5$. This is because $F(x_1, x_2)$ always visits the range $[-0.5, 0.5]$ in a perfectly synchronized manner with the interoceptive input, as shown in Fig. 2, leading to the overestimation of the expected value of the stochastic perceptual alternation shown in Fig. 2-(b). We collected the phase of the interoceptive signal $g(t)$ or $A(t)$ when the state of a WTA transitioned among these three states, and computed the probability density shown in Fig. 3 and 4.

WTA behavior driven by the additive input signal $A(t)$ with normal and small activation gain g_b

We analyze how interoceptive common input $A(t)$ affect the behavior of a WTA circuit. If the acitivation gain $g(t)$ in Eq. 1 is constant and small as $g_g = 0$ and $g_b \sim 0$, the WTA neurons have rather linear dynamics, then Eq. 1 is reduced to the following one-dimensional dynamics with respect to $\tilde{X}$ as

$$\frac{d\tilde{X}}{dt} = -\tilde{X} - \frac{g_b}{4}\tilde{W}\tilde{X} + \sqrt{2D}\xi(t), \tag{S1}$$

where $\tilde{X} = x_1 - x_2$ and $\tilde{W} = \left(w_{ii} - w_{ij}\right)$. Eq. S1 indicates that in the linear WTA regime (i.e., $g_b \ll 1$), the interoceptive common input $A(t)$ does not contribute to the dynamics of the neural state transition. For additional supporting material, please refer to Fig. S3-(b).

Fig. S2 shows the WTA behavior driven by the additive input signal $A(t) = A_g(t)\sin(2\pi f t) + A_b$, with the normal activation gain $g_b = 1.5$ (A), and the small gain $g_b = 0.1$ (B). Note that the red line denotes $f(x_1)$ (the output of x_1), and the blue line denotes $f(x_2)$. Black line in the panel (B) denotes $f(x_1) - f(x_2)$, and it is shown $f(x_1) - f(x_2) \sim 0$, and the WTA loses the bistability.

Detail analysis of the effect of interoceptive additive input to WTA

To analyze the effect of interoceptive input $A(t)$ in Eq. 1, we use Itô's formula (*40*). Eq. 1 can be written in the following differential form as

$$dx_i(t) = \left(-x_i + w_{ij} f\left(x_j\right) + w_{ii} f\left(x_i\right) + A\left(t\right)\right) dt + \eta_i dB_{i,t}, \tag{S2}$$

and, furthermore, in the integral form as

$$x_i(t) = x_i(0) + \int_0^t \left(-x_i + w_{ij} f\left(x_j\right) + w_{ii} f\left(x_i\right) + A\left(t\right)\right) dt + \int_0^t \eta dB_{i,t}, \tag{S3}$$

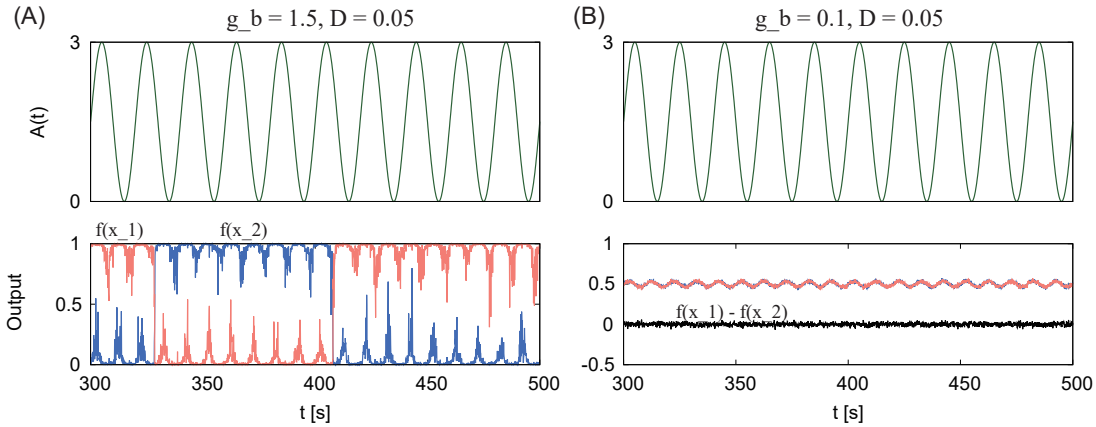

Figure S2: **WTA behavior in response to the additive input signal $A(t)$ with moderate activation gain $g_b = 1.5$. (A)**, and small activation gain $g_b = 0.1$ **(B)**. It is shown that with moderate g_b, WTA exhibits bistable behavior and stochastic switching behavior based on the input $A(t)$. The bistability is lost for small g_b, and in this parameter regime, $f(x_1) - f(x_2) \sim 0$. We used $D = 0.05$.

where (i, j) is either $(1, 2)$ or $(2, 1)$, $\eta = \sqrt{2D}\xi$ and $dB_{i,t}$ describes the path of noise process (note that we assumed $\tau = 1$ for simplicity). Because the Talor expansion of $f(x_i + dx_i)$ is described as

$$f(x_i + dx_i) = f(x_i) + \frac{\partial f}{\partial x_i} dx_i + \frac{1}{2}\frac{\partial^2 f}{\partial x_i^2}(dx_i)^2. \tag{S4}$$

Because $df(x_i) = f(x_i + dx_i) - f(x_i)$, we have the differential form of $f(x_i)$ as follows:

$$df(x_i) = \frac{\partial f}{\partial x_i} dx_i + \frac{1}{2}\frac{\partial^2 f}{\partial x_i^2}(dx_i)^2 = \frac{\partial f}{\partial x_i} dx_i + \frac{1}{2}\frac{\partial^2 f}{\partial x_i^2}\eta^2 dB_{i,t}. \tag{S5}$$

Note that in the limit $dt \to 0$, $(dB_t)^2 \to 0$, $dB_t dt \to 0$, $dt^2 \to 0$, and $dx_i^2 \to \eta^2 dB_{i,t}$ *(40)*.

By substituting Eq. S2 to Eq. S5, and taking the integral of $df(x_i)$, we have the integral form of Eq. S5

$$\begin{aligned} f(x_i) =& \frac{\partial f}{\partial x_i}\int_0^t \left(-x_i + w_{ii} f(x_i) + w_{ij} f(x_j) + A(s)\right) ds \\ &+ \frac{1}{2}\frac{\partial^2 f}{\partial x_i^2}\int_0^t \eta^2 ds + \frac{\partial f}{\partial x_i}\int_0^t \eta dB_{i,t} + f(x_i(0)). \end{aligned} \tag{S6}$$

We can compute $F(x_1, x_2) = f(x_1) - f(x_2)$ as

$$F(x_1, x_2) = C + \int_0^t (H(x_1, x_2))\, ds + \frac{1}{2}\Delta_f^2 \int_0^t \eta^2(s) ds$$
$$+ \Delta_f \left(\int_0^t \eta dB_t + \int_0^t A(s) ds \right), \tag{S7}$$

where $C = F(x_1(0), x_2(0))$, $\Delta_f = \partial f/\partial x_i - \partial f/\partial x_j$, $\Delta_f^2 = \partial^2 f/\partial x_i^2 - \partial^2 f/\partial x_j^2$, $H(x_1, x_2) = K(x_1) - K(x_2)$, and furthermore, $K(x_i) = \int_0^t \frac{\partial f}{\partial x_i} \left(-x_i + w_{ii} f(x_i) + w_{ij} f(x_j)\right) ds$. Taking the Taylor expansion of Eq. S7 around $x_1 = 0$ and $x_2 = 0$, we have the result shown in Eq. 4. It should be noted that the dependency of $F(x_1, x_2)$ on $A(s)$ disappears when we take the Taylor expansion around $g = 0$.

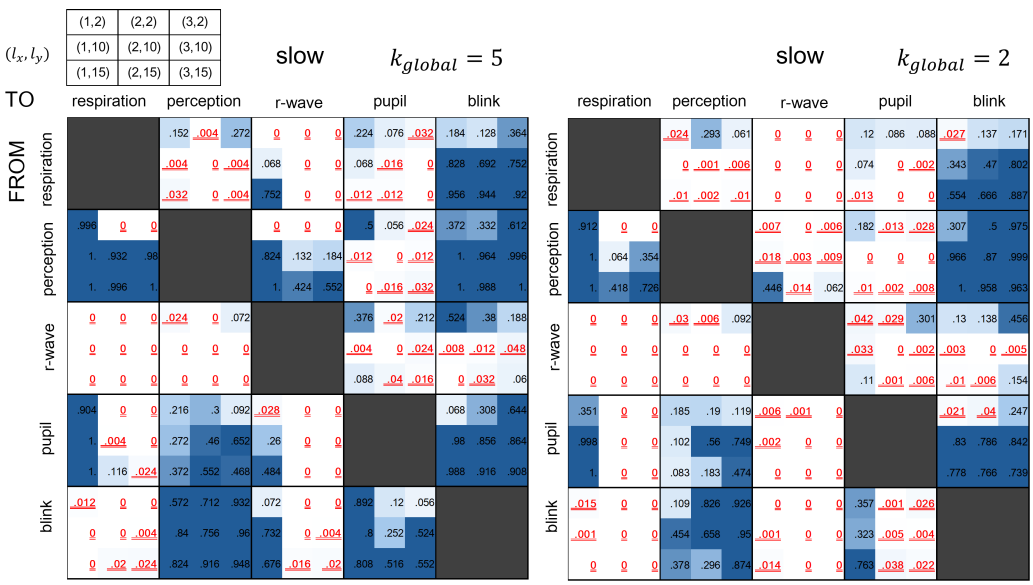

Figure S3: **The heatmap shows the p-values obtained by means of the permutation test using transfer entropy (TE) between the respiration phase θ, the timing of the perception alternation e_p, the R-wave, R, the normalized pupil diameter d_p, and the blink timing B_l in the slow respiration rate.** We used $k_{global} = 5$ and $k_{global} = 2$ to calculate TE. Furthermore, we used $k_{perm} = 100$ for $k_{global} = 2$. The 3×3 submatrix denotes the embedding dimension l_x, l_y used to compute TE from $y \to x$ (y and x are the source and target processes, respectively). The p-values which satisfy the condition < 0.05 are indicated by blue fonts with a double underline.

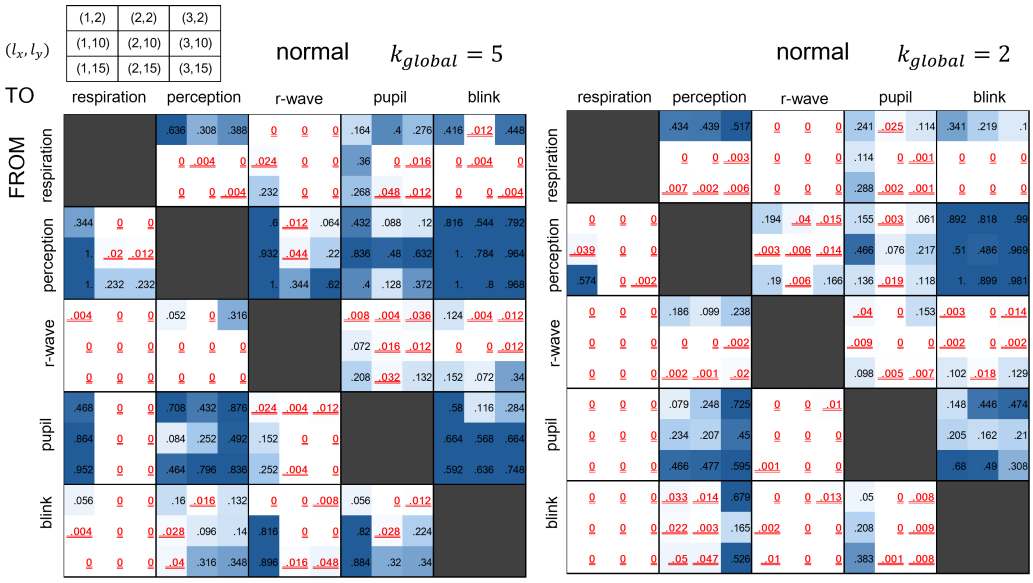

Figure S4: **The heatmap shows the p-values obtained by means of the permutation test using transfer entropy (TE) between the respiration phase θ, the timing of the perception alternation e_p, the R-wave, R, the normalized pupil diameter d_p, and the blink timing B_l in the normal respiration rate.** We used $k_{global} = 5$ and $k_{global} = 2$ to calculate TE. Furthermore, we used $k_{perm} = 100$ for $k_{global} = 2$. The 3×3 submatrix denotes the embedding dimension l_x, l_y used to compute TE from $y \rightarrow x$ (y and x are the source and target processes, respectively). The p-values which satisfy the condition < 0.05 are indicated by blue fonts with a double underline.

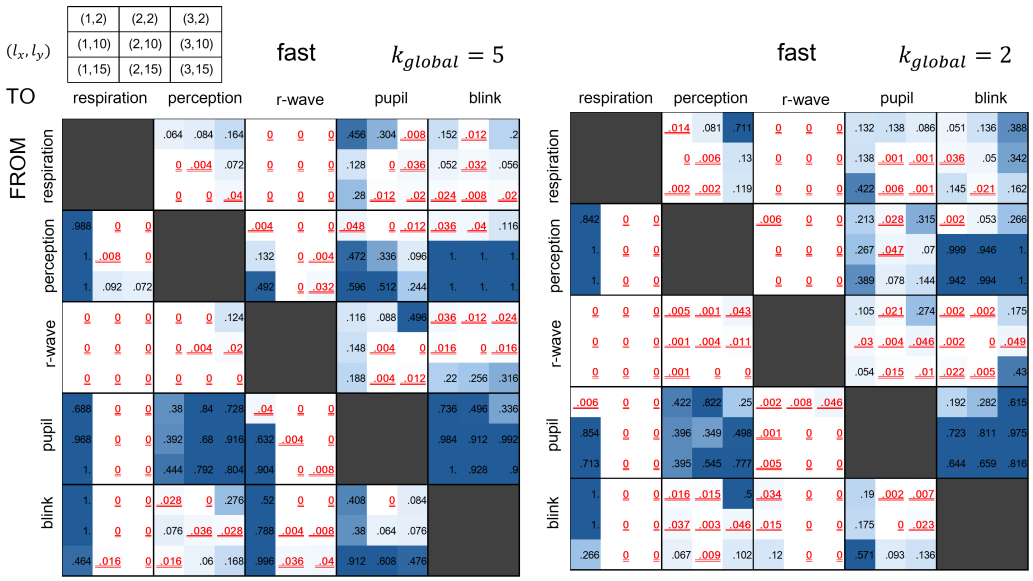

Figure S5: **The heatmap shows the p-values obtained by means of the permutation test using transfer entropy (TE) between the respiration phase θ, the timing of the perception alternation e_p, the R-wave, R, the normalized pupil diameter d_p, and the blink timing B_l in the fast respiration rate.** We used $k_{global} = 5$ and $k_{global} = 2$ to calculate TE. Furthermore, we used $k_{perm} = 100$ for $k_{global} = 2$. The 3×3 submatrix denotes the embedding dimension l_x, l_y used to compute TE from $y \rightarrow x$ (y and x are the source and target processes, respectively). The p-values which satisfy the condition < 0.05 are indicated by blue fonts with a double underline.